

## Electronic Supplementary Information

# Suppression of Marangoni effect by controlling the mixing procedures of the precursor solution to improve the performance of perovskite solar cells

*Yunfei Wang,<sup>ab</sup> Lili Shen,<sup>a</sup> Xinyu Chen,<sup>a</sup> Zongqi Chen<sup>a</sup> and Songwang Yang<sup>\*ab</sup>*

*<sup>a</sup>CAS Key Laboratory of Materials for Energy Conversion, Shanghai Institute of Ceramics, Chinese Academy of Sciences, 588 Heshuo Road, Shanghai 201899, China. E-mail: swyang@mail.sic.ac.cn*

*<sup>b</sup>Center of Materials Science and Optoelectronics Engineering, University of Chinese Academy of Sciences, Beijing 100049, China.*

## **Materials**

Ethanol (EtOH, 95%) and  $\gamma$ -valerolactone (GVL, 98%) were purchased from Aladdin Reagent Co. Lead iodide ( $\text{PbI}_2$ , 99.99%) was purchased from Xi'an Polymer Light Technology Corp. Methylammonium iodide (MAI, 99.9%) and 5-aminovaleric acid iodide (5-AVAI) were purchased from Greatcell Solar. Fluorine-doped tin oxide (FTO, A22-8A,  $8\Omega/\text{sq}$ ) were purchased from Asahi Glass Co. Ltd. All chemicals were used without further purification.

$\text{TiO}_2$ ,  $\text{ZrO}_2$  and carbon pastes for screen printing were prepared in-house according to the previous paper<sup>1</sup>. Typically, for the  $\text{TiO}_2$  (20 nm) and  $\text{ZrO}_2$  (50 nm) pastes, 1g of powder was first mixed with 20 mL of ethanol, 0.5 g of ethyl cellulose, and 5 g of terpineol. Then they were homogenized with ultra-sonification and ball milling. Finally, the ethanol was removed by rotary evaporator to obtain the desired pastes. For the carbon paste, 6 g of graphite, 2 g of carbon black, 1g of  $\text{ZrO}_2$  nanoparticle (50 nm), and 1 g of ethyl cellulose were mixed with 30 mL of terpineol by ball milling for 10 h.

## **Preparation of perovskite precursor solution**

The control solution (conventional mixing procedure). The required amount of powders (0.476 g  $\text{PbI}_2$ , 0.195 g MAI, 0.0076 g 5-AVAI) were added into the bottle. Then the mixed solvent of  $\gamma$ -valerolactone (0.8 mL) and ethanol (0.2 mL) in a volume ratio of 4:1 was added into the bottle. Finally, a 1.03 mol/L control solution was obtained.

The target solution (optimized mixing procedure). The required amounts of 5-ammonium valeric acid iodide (0.0076 g) powder and methylamine iodide (0.195 g) powder were first added to the bottle in sequence, followed by adding the mixed solvent of  $\gamma$ -valerolactone (0.8 mL) and ethanol (0.2 mL) in a 4:1 volume ratio. Then, the desired amount of lead iodide (0.476 g) was added immediately after the solids had dissolved. Finally, a 1.03 mol/L target solution was obtained.

## **Fabrication of printable mesoscopic perovskite solar cells**

The FTO glass substrates were laser etched to delineate the positive and negative areas and cleaned sequentially in detergent, deionized water, and ethanol for 60 min. Subsequently, c- $\text{TiO}_2$  layer, m- $\text{TiO}_2$  layer, m- $\text{ZrO}_2$  layer, and carbon layer were sequentially printed using screen

printing. Silver (Ag) was then printed as the electrode material on the positive and negative terminals of the cell. The positional relationship between the layers is shown in Fig. S20a. Before depositing the next layer, each layer was dried at 100°C for 10 min and sintered at 510°C for 30 min, with the exception of the carbon layer, which was sintered at 430°C for 30 min. The m-TiO<sub>2</sub> layer had a thickness of 800-1000 nm, the m-ZrO<sub>2</sub> layer had a thickness of 2.2-2.3 μm, and the carbon layer had a thickness of 35-40 μm. Within 60 min after the carbon layer sintering, 5.4 μL of perovskite solution was drop-coated onto the carbon layer and then annealed at 63 °C for 120 min. The corresponding effective area is 0.9 cm<sup>2</sup> and the annealing process requires a controlled ambient humidity between 30% and 50%.

### **Fabrication of printable mesoscopic perovskite solar sub-modules**

The sub-module has an effective area of 66 cm<sup>2</sup>. The fabrication process for the sub-module, including the perovskite deposition and annealing, was consistent with that of the small-sized cells. The sub-module consists of twelve cells connected in series, and the layer structure within each cell is the same as in the small-sized devices. For each cell, 29.7 μL of perovskite solution was applied dropwise using an inline pipette gun. To achieve the series connection of the twelve cells, several steps were implemented: an insulating area (P<sub>1</sub>: 0.7 mm) was laser-etched to prevent short circuits between the negative electrodes (the wavelength of the laser used is 532nm and the power is 1.5 W); a blank area (0.1 mm) was left during the screen printing process to prevent the positive and negative electrodes of adjacent cells from connecting; and another blank area (1 mm) was left to prevent the positive electrodes of adjacent cells from connecting. The positional relationship of these areas and the sub-module dimensions are illustrated in Figs. S20 b and c.

## **Characterization**

### **Measurements of the photovoltaic performance**

Photovoltaic performance was measured using a solar simulator (Yamashita Denso YSS-150A, Japan) with a standard silicon solar cell (MH66504, Minghe Photovoltaic Technology Co., Ltd., China) under 1 sun illumination (AM 1.5G, 100 mW/cm<sup>2</sup>). The J-V characteristic curve was scanning from high to low potential. For the measurement of a 0.07 cm<sup>2</sup> masked cell (1.5 × 2.5

cm<sup>2</sup> outer area), a mask with the aperture area of 0.07 cm<sup>2</sup> was used with the following parameters: a voltage scan range of -0.1 to 1.2 V, a maximum scanning current of 0.01 A, and 51 scanning points. For the cell with the active area of 0.9 cm<sup>2</sup> without a mask: a voltage scan range of -0.1 to 1.5 V, a maximum scanning current of 0.03 A, and 51 scanning points. For submodule measurements, no mask was required, and the voltage scan range was -0.1 V to 13 V, with a maximum current of 0.3 A. All the measurements included a 30 second light soaking period prior to data acquisition.

### **Measurements of the <sup>1</sup>H-NMR**

<sup>1</sup>H-NMR tests were performed using a Bruker Ascend TM 600 MHz NMR spectrometer. A perovskite precursor solution, diluted 1:10 in deuterated DMSO (DMSO-d<sub>6</sub>), was used for the <sup>1</sup>H-NMR analysis. When calibrating the <sup>1</sup>H-NMR spectrum, the characteristic peaks of DMSO-d<sub>6</sub> must be calibrated first.

### **Measurements of the HRMS**

High-resolution mass spectrometry (HRMS) analysis of the precursor solutions was performed in electrospray ionization (ESI) mode using a Bruker ESI-Q-TOF MS/MS high-resolution mass spectrometer.

### **Measurements of the IPCE**

Incident Photon-to-Current Efficiency (IPCE) measurements for the perovskite solar cell devices were performed using a Bunkoukeiki CEP-1500 monochromatic photoelectric converter in the wavelength range of 300 to 850 nm, with a step size of 20 nm.

### **Measurements of the Electroluminescence**

High-resolution electroluminescence images were obtained by using an infrared camera in a dark environment at 25°C with a DC voltage of 11 V applied to the PSCs. The camera parameters need to be adjusted to obtain clear images. The camera was made by Suzhou Lexus New Energy Technology Co.

### **Measurements of the SEM**

Scanning electron microscope (SEM) images were acquired using an FEI Magellan 400 field emission scanning electron microscope. The test samples were prepared by slicing the perovskite solar cell to expose its cross-section for observation.

### **Measurements of GIWAXS**

GIWAXS testing on the BL14B1 line at the Shanghai Synchrotron Radiation Facility (SSRF).

### **Measurements of contact angle and surface tension**

Contact angle and surface tension were determined using a Chengde Dingsheng JY-82C contact angle/surface tension analyzer. The static contact angle of the perovskite precursor solution on the substrate, the dynamic contact angle during spreading on the substrate, and the surface tension of the perovskite precursor solution were measured.

### **Measurements of the storage stability**

The device was stored in a dark environment at a relative humidity between 25% and 35%, and its J-V curve was tested at regular intervals.

## Supplementary Note 1:

The  $^1\text{H}$  peak at  $\sim 12.05$  ppm belongs to the hydroxyl hydrogen of 5-AVA. Combining samples 3-8, which were carefully analyzed using sample 8 as a standard, it can be seen that the chemical shift of sample 6 is larger than that of sample 8, while that of sample 4 is smaller than that of sample 8, which proves that MA increases the chemical shift of 5-AVA while Pb decreases the chemical shift of 5-AVA. The chemical shifts of sample 6 are comparable to that of sample 1 and sample 4 is comparable to that of sample 2, suggesting that the action of Pb on 5-AVA is superior to that of MAI, and on this basis, combined with the fact that the chemical shift of sample 3 is smaller than that of sample 8, it can be surmised that there is also a mechanism for increasing the chemical shift of carboxy hydrogen between 5-AVA and EtOH. Next, by comparing the calibration results with the predicted chemical shifts of the known substances, an additional quadruple-split peak was found with a chemical shift of 4-4.02 ppm (Fig. S12a) and an additional triple-split peak at 1.14-1.17 ppm (Fig. S12b). These two peaks correspond to the two hydrogens of the ethyl ester functional group present in the presence of 5-AVA and EtOH. Therefore, it can be reasonably assumed that the esterification reaction between 5-AVA and EtOH produced ethyl 5-aminopentanoate, which explains why the interaction between 5-AVA and EtOH increased chemical shifts of the carboxylic acid hydrogens. The fragment detected by high-resolution mass spectrometry for sample 6 in Fig. S12c is also consistent with the predicted result in Fig. S13, proving that the esterification reaction took place.

The peak at 7.4-7.7 ppm belongs to the active hydrogen in the amino group (Fig. S15a), which is susceptible to interferences in chemical environments and changes in chemical shifts, but it can be concluded that it is the same in the same environment, and it can be inferred that the peak at 7.5-7.7 ppm belongs to the  $-\text{NH}_2$  in 5-AVA, 7.4-7.6 ppm belongs to the  $\text{NH}_2$  in MA, and the 7.4-7.6 ppm peak belongs to the  $-\text{NH}_2$  in MA.  $\text{NH}_2$  in MA, 7.4-7.6 ppm peaks belong to  $-\text{NH}_2$  in MA, and hydrogen in MA belonging to the amino group seems to be increased in sample 6. Comparing sample 6 with other compositions, it can be concluded that the interaction of MA with 5-AVA leads to a general increase in the chemical shifts of the amino hydrogens in MA, but this process is also influenced by Pb. Combined with the esterification reaction that occurred in sample 6 above, it can be assumed that this process is also related to the

esterification process, and the change in chemical shift of the methyl hydrogen of MA in Fig. S15 b proves this point. In Fig. S15b, MA was present with EtOH (sample 7), MAI, Pb, and EtOH (sample 5), and the co-presence of Pb, MAI, and 5-AVA did not cause the chemical shift of the methyl hydrogen. The co-presence of Pb, MAI, and 5-AVA does not cause chemical shifts of the methyl hydrogen, whereas the co-presence of MAI, 5-AVA, and EtOH increases their chemical shifts, so it can be hypothesized that the interaction process between MAI and 5-AVA should involve EtOH, whereas the presence of Pb inhibits this process.

5-AVA has shown to esterify with EtOH to form ethyl 5-aminovalerate (Et-5AVR), so it is assumed that the increase in chemical shift of MA is due to the reaction of MA with Et-5AVR, which can be confirmed by the fact that control sample has a smaller chemical shift than the target sample and sample 6 (which are identical and the esterification takes place undisturbed in both samples). The chemical shift of the amino hydrogen in sample 6 increased from 7.5 ppm to 7.6 ppm, suggesting that Et-5AVR was esterified with MA to form an amide. When reacting with MA to form 5-amino-N-methylpentanamide (P-5ANM), the <sup>1</sup>H-NMR results predicted by ChemDraw (Fig. S14) are in good agreement with the actual calibration results, and the same can be observed from the high-resolution detection of sample 6 in Fig. S15 c. The fragment in Fig. S16 agrees with the predicted results, proving that the amidation reaction has taken place.

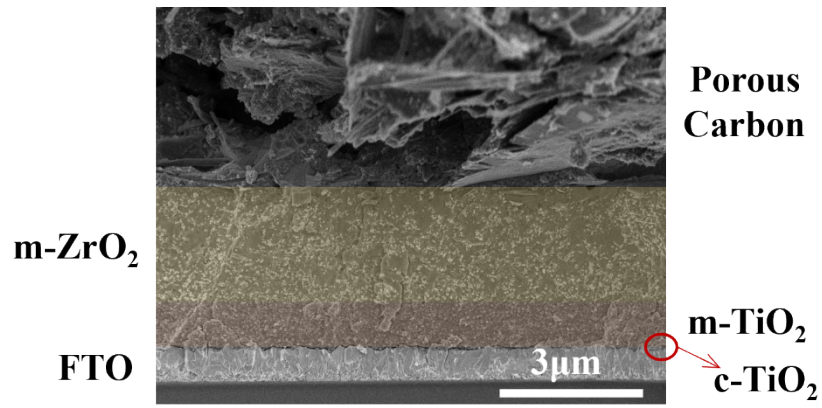


Fig S1. Cross-sectional SEM image of the perovskite solar cell.

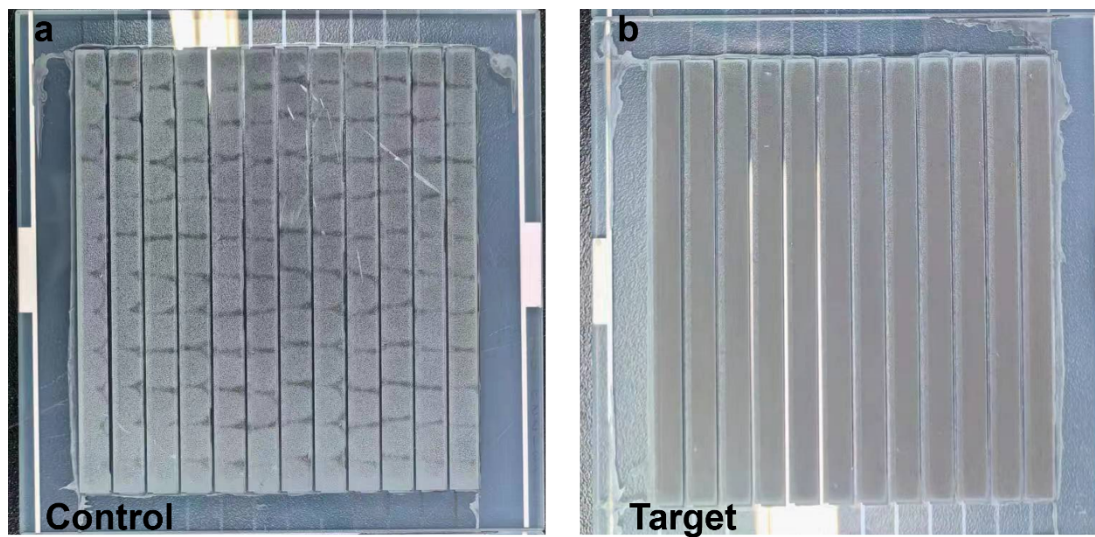


Fig S2. Pictures of (a) the Control and (b) the Target devices

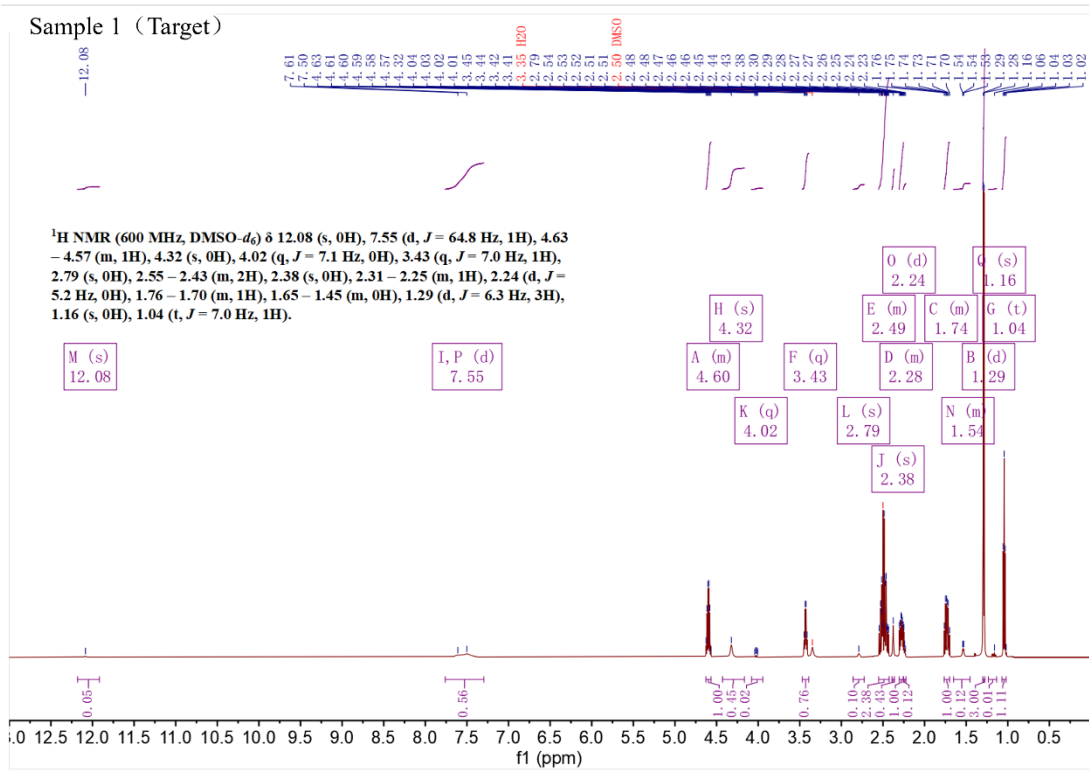


Fig S3. <sup>1</sup>H-NMR (DMSO-*d*<sub>6</sub>) of sample 1 (the target solution).

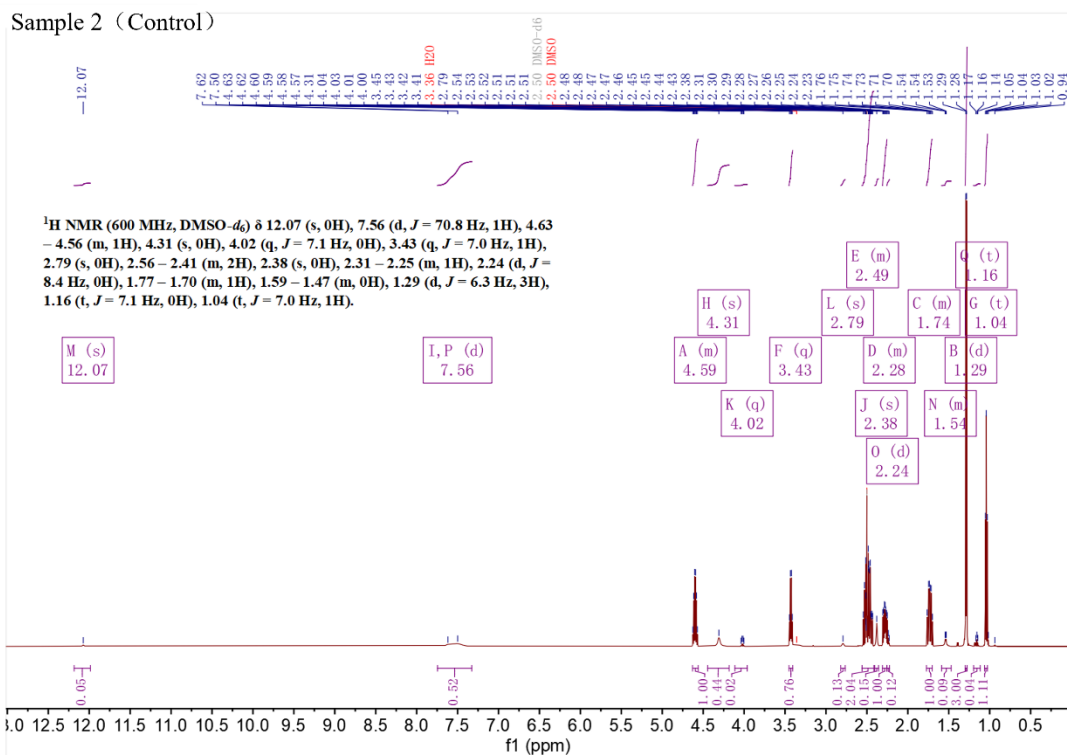


Fig S4. <sup>1</sup>H-NMR (DMSO-*d*<sub>6</sub>) of sample 2 (the control solution)

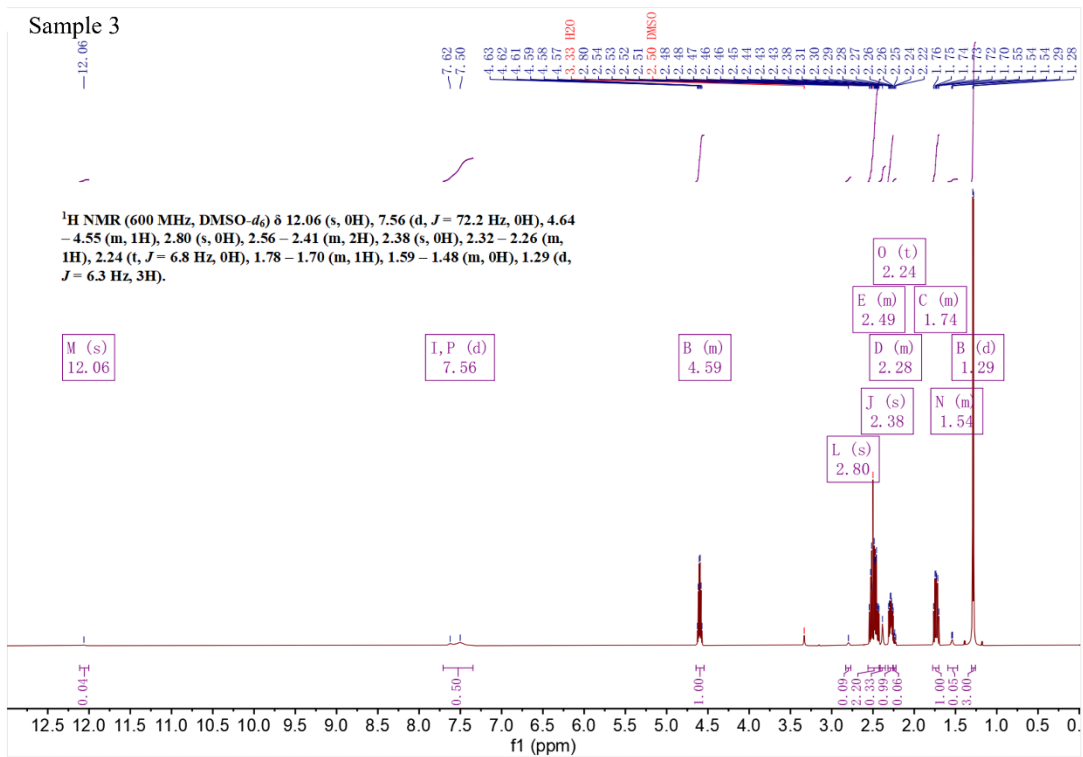


Fig S5. <sup>1</sup>H-NMR (DMSO-d<sub>6</sub>) of sample 3.

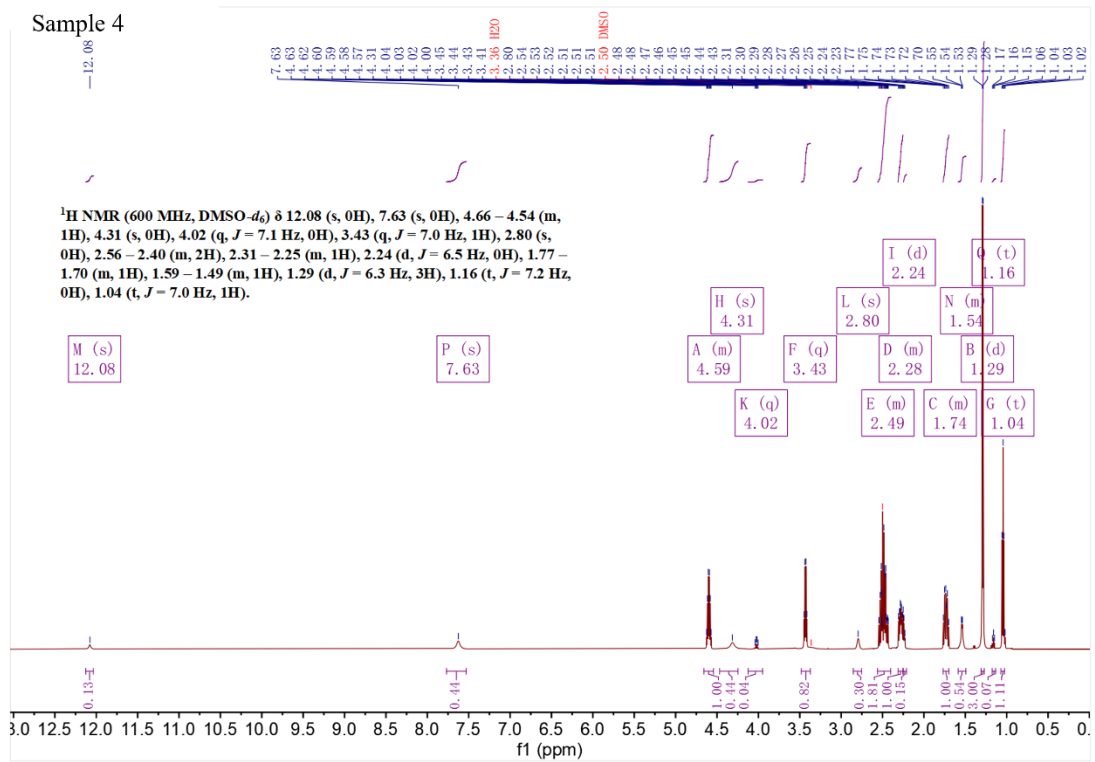


Fig S6. <sup>1</sup>H-NMR (DMSO-*d*<sub>6</sub>) of sample 4.

Sample 5

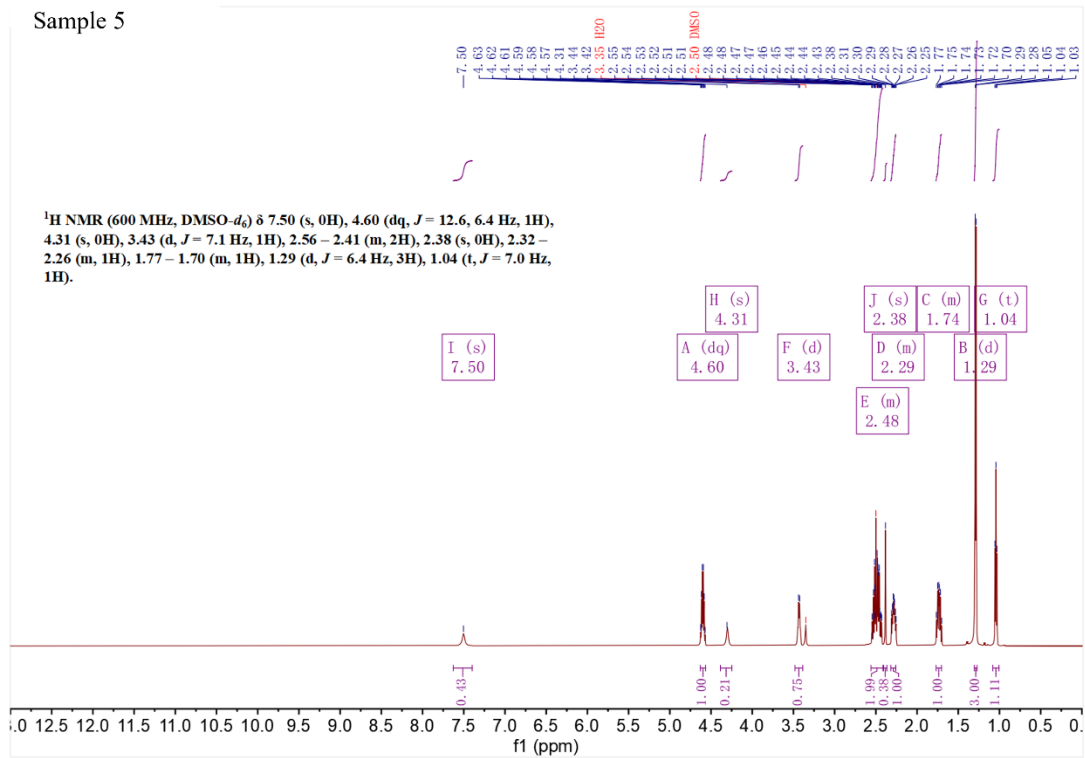


Fig S7. <sup>1</sup>H-NMR (DMSO-*d*<sub>6</sub>) of sample 5.

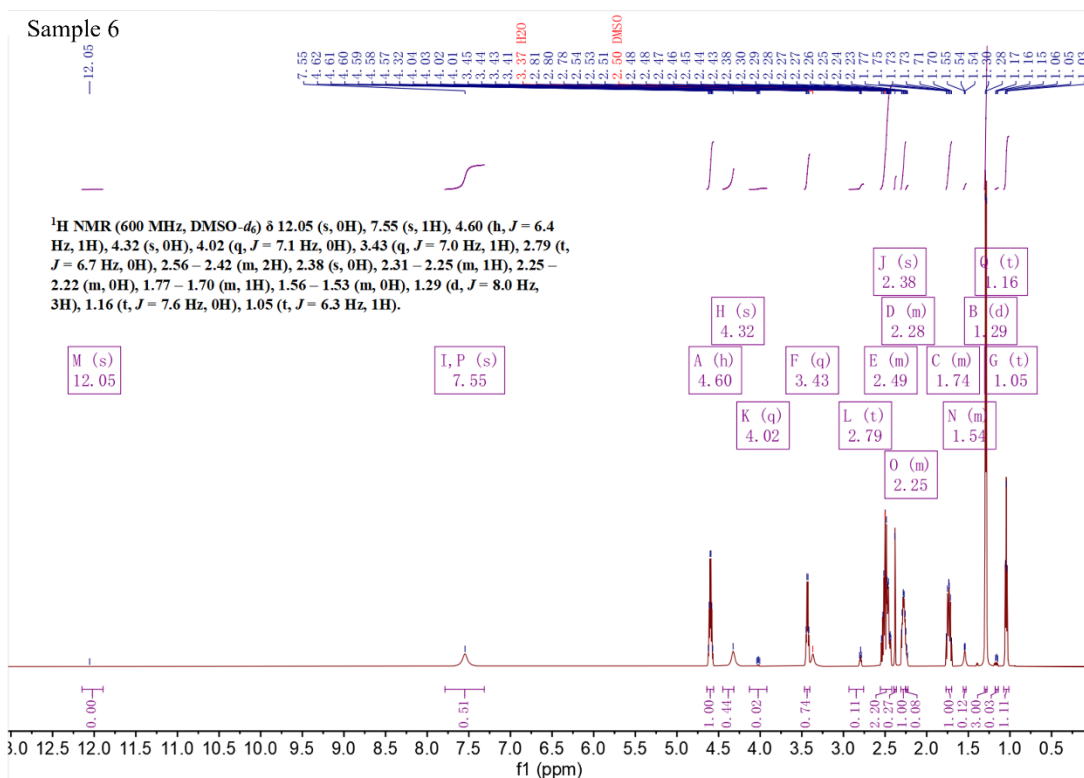


Fig S8. <sup>1</sup>H-NMR (DMSO-*d*<sub>6</sub>) of sample 6.

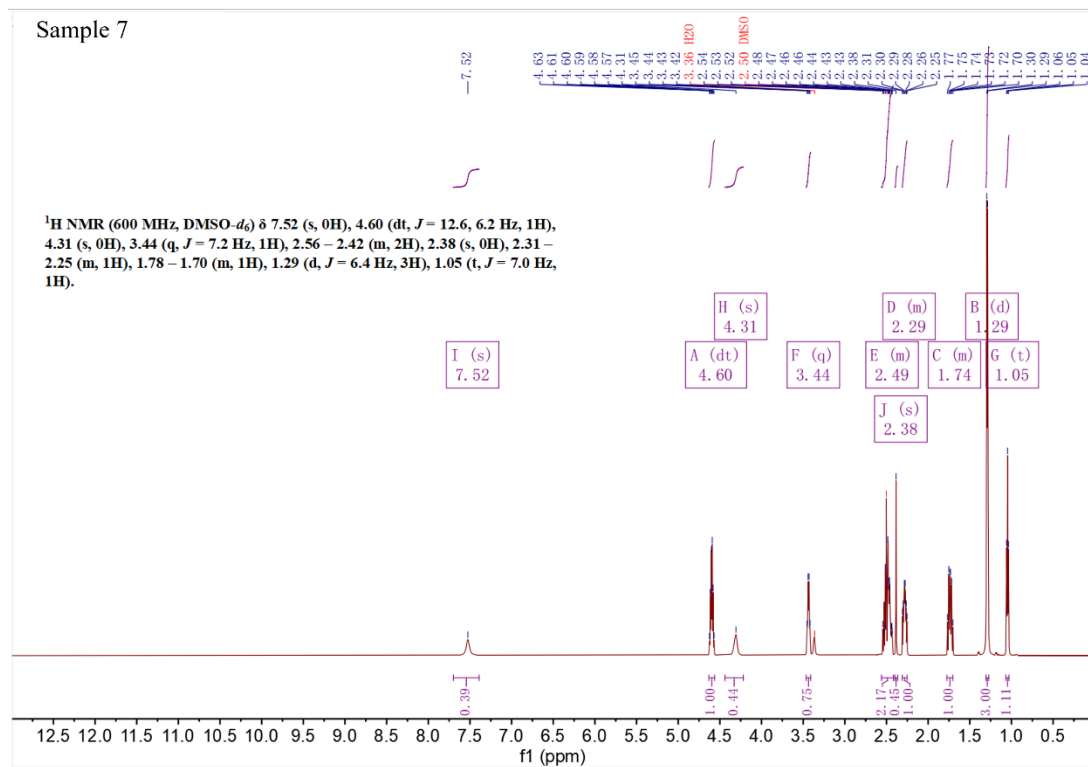


Fig S9. <sup>1</sup>H-NMR (DMSO-d<sub>6</sub>) of sample 7.

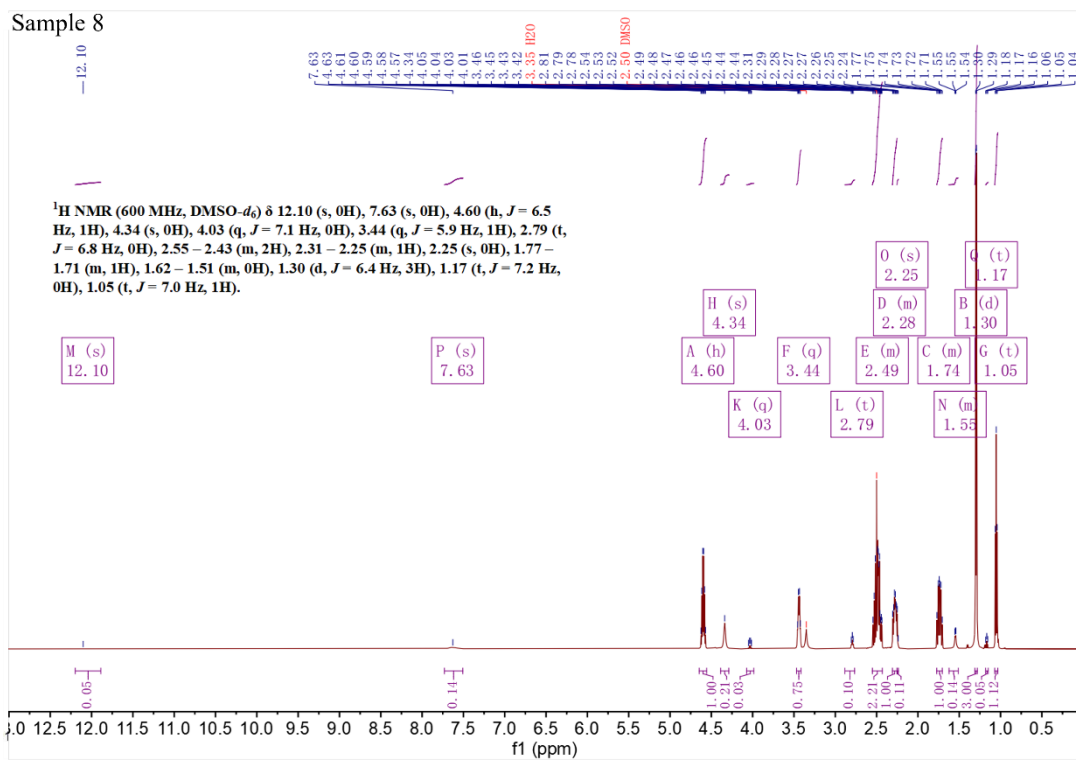
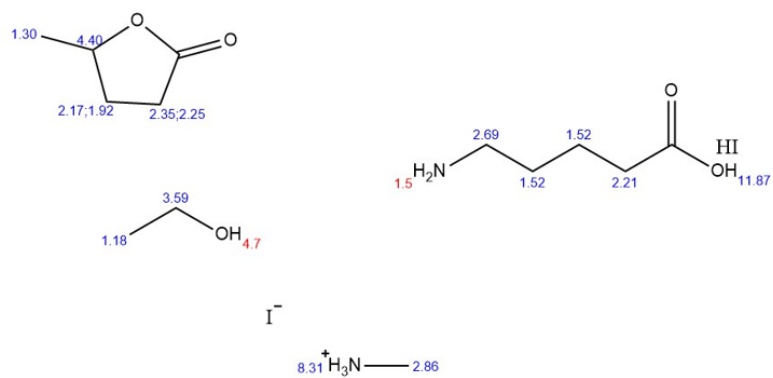


Fig S10. <sup>1</sup>H-NMR (DMSO-*d*<sub>6</sub>) of sample 8

### ChemNMR $^1\text{H}$ Estimation



Estimation quality is indicated by color: **good**, **medium**, **rough**

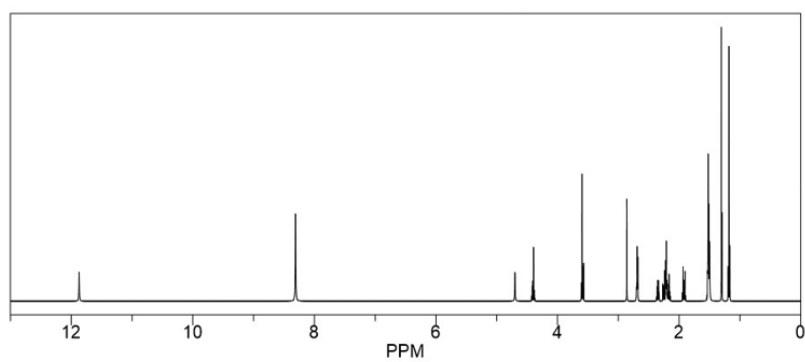


Fig S11. Simulation of  $^1\text{H}$ -NMR (DMSO- $d_6$ ) of MAI, EtOH, GVL, and 5-AVAI.

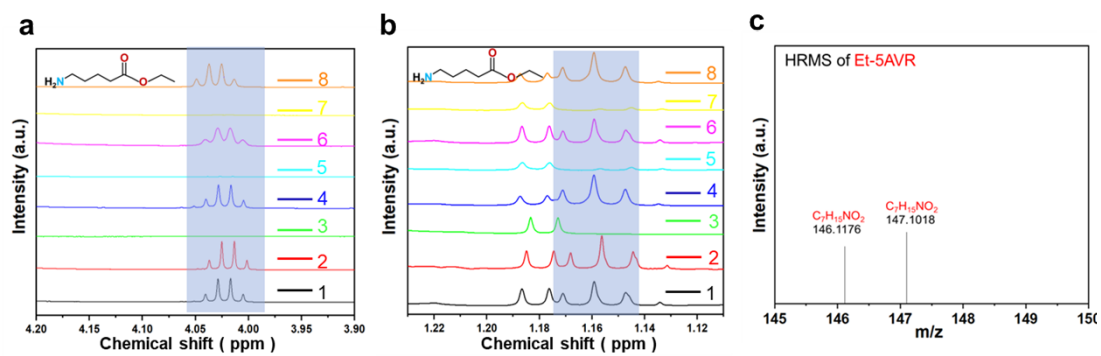


Fig S12. Comparative analysis of  $^1\text{H}$ -NMR in 1-8 groups of solutions and verification of HRMS. (a and b) The chemical shift changes of  $^1\text{H}$  peak in Et-5AVR. (c) High Resolution Mass Spectrometry of Et-5AVR.

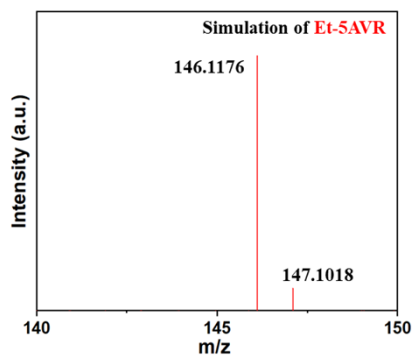
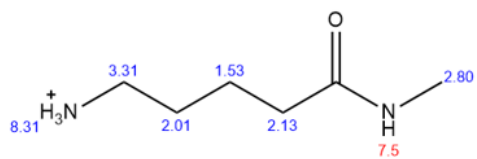


Fig S13. Simulation of High-Resolution Mass Spectrometry of Et-5AVR.

## ChemNMR $^1\text{H}$ Estimation



Estimation quality is indicated by color: **good**, **medium**, **rough**

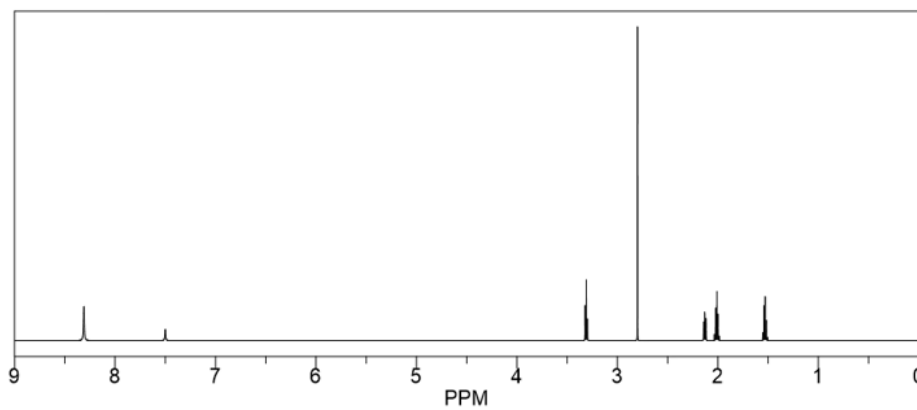


Fig S14. Simulation of  $^1\text{H}$ -NMR (DMSO- $d_6$ ) of 5-amino-N-methyl- Pentanamide (P-5ANM).

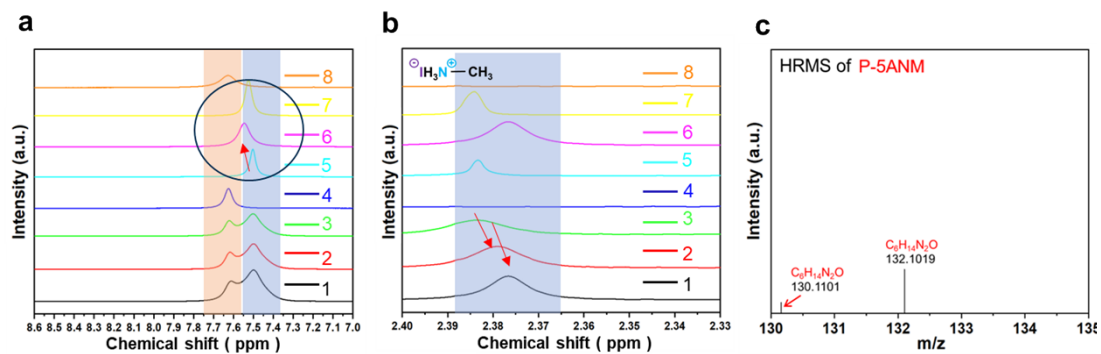


Fig S15. Comparative analysis of  $^1\text{H-NMR}$  in samples 1-8 and verification of HRMS. (a and b) The chemical shift changes of  $^1\text{H}$  peak in MAI. This change illustrates the generation of 5-amino-N-methyl-pentanamide (P-5ANM) (c) High Resolution Mass Spectrometry of P-5ANM.

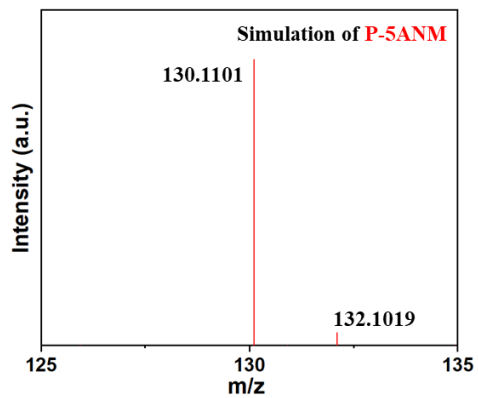


Fig S16. Simulation of High-Resolution Mass Spectrometry of P-5ANM.

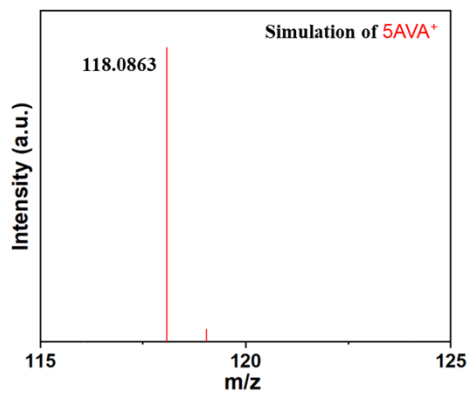


Fig S17. Simulation of High-Resolution Mass Spectrometry of 5-AVA<sup>+</sup>.

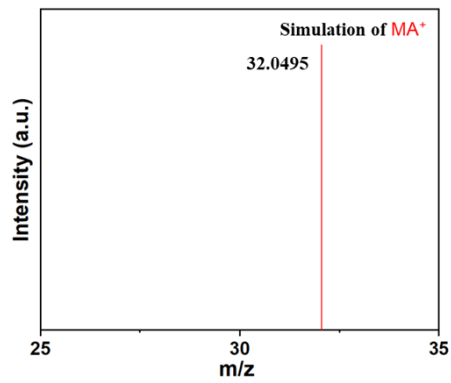


Fig S18. Simulation of High-Resolution Mass Spectrometry of MA<sup>+</sup>.

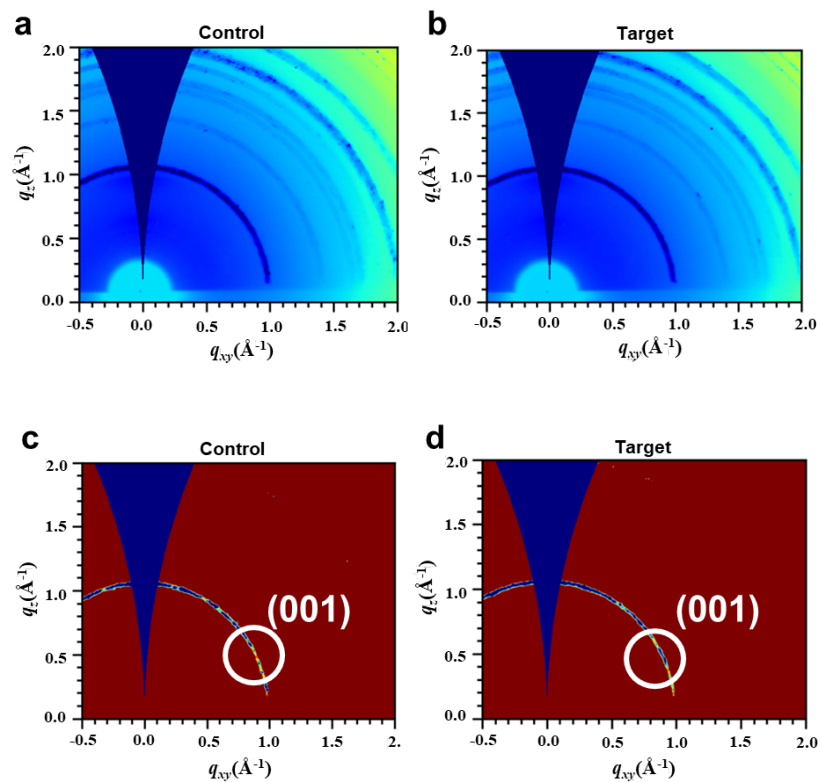


Fig S19. (a and b) GIWAXS of crystals from the control and target films. (c and d) GIWAXS of (001) crystal plane of the control and target films.

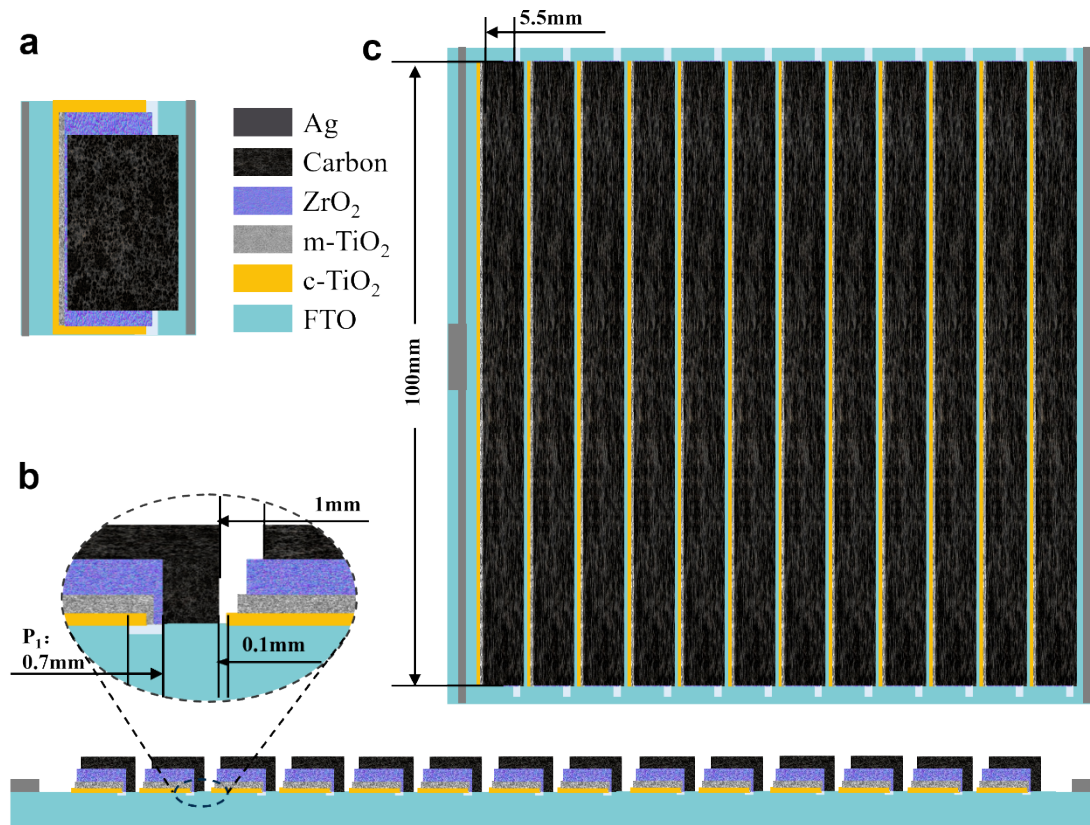


Fig S20. Detailed dimensional information for the sub-module. (a) Positional relationship between layers (b) Dimensions of each region (c) Dimensions of the sub-module.

**Table S1.** The composition of the control/target solution and the preparation method.

	<b>Sample</b>	<b>Composition</b>	<b>Method</b>
<b>Target</b>	— 1	MAI+5-AVAI+PbI <sub>2</sub> +GVL+EtOH	Optimized
<b>Control</b>	— 2	MAI+5-AVAI+PbI <sub>2</sub> +GVL+EtOH	Conventional

**Table S2.** Compositions of Samples 3-8.

<b>Sample</b>	<b>Composition</b>
— 3	PbI <sub>2</sub> +MAI+5-AVAI+GVL
— 4	5-AVAI+PbI <sub>2</sub> +GVL+EtOH
— 5	MAI+PbI <sub>2</sub> +GVL+EtOH
— 6	MAI+5-AVAI+GVL+EtOH
— 7	MAI+GVL+EtOH
— 8	5-AVAI+GVL+EtOH

**Table S3.** Performance development of (5-AVA)<sub>x</sub>(MA)<sub>1-x</sub>PbI<sub>3</sub> C-PSC.

Year	Device structure	$V_{oc}$ (V)	$J_{sc}$ (mA/cm <sup>2</sup> )	FF (%)	PCE (%)	Ref
2013	FTO/c-TiO <sub>2</sub> /mp-TiO <sub>2</sub> /mp-ZrO <sub>2</sub> /Carbon	0.88	10.60	61	6.6	<i>Sci Rep</i> 3, 3132(2013) <sup>2</sup>
2014	FTO/c-TiO <sub>2</sub> /mp-TiO <sub>2</sub> /mp-ZrO <sub>2</sub> /Carbon	0.86	22.80	66	12.8	<i>Science</i> 345, 295(2014) <sup>3</sup>
2015	FTO/c-TiO <sub>2</sub> /mp-TiO <sub>2</sub> /mp-ZrO <sub>2</sub> /Carbon	0.87	22.90	67	13.4	<i>J. Mater. Chem. A</i> 3, 9103(2015) <sup>4</sup>
2017	FTO/c-TiO <sub>2</sub> /mp-TiO <sub>2</sub> /mp-ZrO <sub>2</sub> /Carbon	0.913	23.02	67	14.0	<i>Sol. RRL</i> 1, 1600019(2017) <sup>5</sup>
2021	FTO/c-TiO <sub>2</sub> /mp-TiO <sub>2</sub> /mp-ZrO <sub>2</sub> /Carbon	0.937	23.62	70	15.5	<i>Sol. RRL</i> 5, 2100333(2021) <sup>6</sup>
2021	FTO/c-TiO <sub>2</sub> /mp-TiO <sub>2</sub> /mp-ZrO <sub>2</sub> /Carbon	0.963	22.37	76	16.3	<i>Adv. Energy Mater</i> 11, 2100292(2021) <sup>7</sup>
2023	FTO/c-TiO <sub>2</sub> /mp-TiO <sub>2</sub> /mp-ZrO <sub>2</sub> /Carbon	0.960	23.83	70	16.06	<i>ACS Appl. Energy Mater</i> 6, 3936-2944(2023) <sup>8</sup>
2024	FTO/c-TiO <sub>2</sub> /mp-TiO <sub>2</sub> /mp-ZrO <sub>2</sub> /Carbon	0.948	24.77	68	16.07	<i>Energy Technol</i> 12, 2301243(2024) <sup>9</sup>

**Table S4.** The statistical photovoltaic parameters for 20 pieces of Control and Target devices

<b>Sample</b>	<b><math>V_{oc}</math> (V)</b>	<b><math>J_{sc}</math> (mA/cm<sup>2</sup>)</b>	<b>FF (%)</b>	<b>PCE (%)</b>
Control	0.909±0.008	24.76±0.35	64.62±0.75	14.53±0.18
Target	0.901±0.021	25.64±0.47	69.62±1.52	16.28±0.27

## References

1. W. Zhang, J. Luo, S. Liu, J. Ma, X. Zhang and S. Yang, *Journal of Inorganic Materials*, 2023, **38**, 213-218.
2. Z. Ku, Y. Rong, M. Xu, T. Liu and H. Han, *Scientific Reports*, 2013, **3**, 3132.
3. A. Y. Mei, X. Li, L. F. Liu, Z. L. Ku, T. F. Liu, Y. G. Rong, M. Xu, M. Hu, J. Z. Chen, Y. Yang, M. Grätzel and H. W. Han, *Science*, 2014, **345**, 295-298.
4. Y. Yang, K. Ri, A. Mei, L. Liu, M. Hu, T. Liu, X. Li and H. Han, *Journal of Materials Chemistry A*, 2015, **3**, 9103-9107.
5. Y. Hu, S. Si, A. Mei, Y. Rong, H. Liu, X. Li and H. Han, *Solar RRL*, 2017, **1**, 1600019.
6. C. Liu, C. Gao, W. Wang, X. Wang, Y. Wang, W. Hu, Y. Rong, Y. Hu, L. Guo, A. Mei and H. Han, *Solar RRL*, 2021, **5**, 2100333.
7. X. Chen, Y. Xia, Q. Huang, Z. Li, A. Mei, Y. Hu, T. Wang, R. Cheacharoen, Y. Rong and H. Han, *Advanced Energy Materials*, 2021, **11**, 2100292.
8. C. Wu, D. Wang, Y. Chen, Z. Zhang, L. Wang, B. She, J. Xiong, W. Xie, Y. Huang and J. Zhang, *ACS Applied Energy Materials*, 2023, **6**, 2936-2944.
9. T. Ding and W. Wu, *Energy Technology*, 2024, **12**, 2301243.